Available online at www.CivileJournal.org

Civil Engineering Journal

(E-ISSN: 2476-3055; ISSN: 2676-6957)

Vol. 11, No. 09, September, 2025

Seismic Response Analysis of Buckling-Restrained Brace Frames Considering Brace Performance Degradation

Qianying Ma [1*], Yu Li [1], Kun Xiong [2*], Chenyang Meng [1], Jiale Zhou [1]

[1] *School of Civil Engineering, Chang'an University, Xi'an 710061, China.*

[2] *School of Earth Science and Resources, Chang'an University, Xi'an 710061, China.*

Received 10 June 2025; Revised 09 August 2025; Accepted 16 August 2025; Published 01 September 2025

Abstract

To elucidate the degradation mechanisms of the hysteretic behavior of buckling-restrained braces (BRBs) in hot–humid service environments and their implications for structural seismic performance, this study tested six BRBs of identical specifications under different numbers of hygrothermal cycles (0, 24, 48, 72, 96, and 120), combining alternating high–low temperature hygrothermal exposure with subsequent quasi-static cyclic loading. The evolution of hysteretic performance parameters with cycle count was quantified. Test results indicate that hygrothermal cycling induces corrosion of the steel core and deterioration of the unbonded material, weakening interfacial bond strength and increasing axial friction effects; consequently, the tensile yield load, elastic stiffness, and ultimate tensile capacity decrease. Based on the experimental observations, a modified Bouc–Wen model was employed to simulate BRB hysteretic nonlinearity, and the identified parameter evolution closely reproduced the measured trends. The degradation model was further incorporated into time-history analyses to assess the influence of BRB performance deterioration on structural response for four representative bracing layouts: single-diagonal (symmetric), single-diagonal (asymmetric), chevron (inverted-V), and multi-story X-braced schemes. All layouts significantly reduced seismic responses; among them, the chevron configuration exhibited the lowest sensitivity to degradation, with response amplification after 120 hygrothermal cycles markedly lower than that of the single-diagonal asymmetric scheme. The findings provide an experimental basis and design reference for seismic design and durability assessment of structures in long-term hot–humid service regions.

Keywords: Buckling-Restrained Brace (BRB); Hygrothermal Cycling; Hysteretic Degradation; Bouc-Wen Model; Seismic Performance.

1. Introduction

Buckling- restrained braces (BRBs) have been widely adopted in the seismic design of both new and existing structures owing to their superior energy dissipation capacity, stable hysteresis, and replaceable construction. By providing effective lateral restraint between the steel core and the outer casing, BRBs suppress compressive buckling of the core, thereby maintaining stable yielding and efficient energy dissipation under tension-compression reversals. Conventional BRBs typically employ a Q235 low-carbon steel core, with concrete or mortar infill supplying external restraint. However, atmospheric exposure in coastal and hot–humid climatic regions induces alternating temperature–humidity cycles accompanied by repeated condensation–drying, capillary sorption, and electrochemical corrosion. These processes drive the synergistic degradation of the steel core, restraining shell, and infill/unbonded materials over the service life. This environmental dimension largely governs the "effective residual capacity" of BRBs during earthquakes. Although prior studies have explored accelerated aging protocols, corrosion-resistant material

* Corresponding author: mqy@chd.edu.cn; xiongkun2003@126.com

http://dx.doi.org/10.28991/CEJ-2025-011-09-09

substitutions, restraint system optimization, and low-cycle fatigue (LCF) constitutive formulations, a systematic, quantitative linkage among "hygrothermal loading → material/interface degradation → hysteretic parameter deterioration → structural response" has yet to be established.

At present, comprehensive investigations that directly target BRB degradation under hygrothermal cycling remain limited. Existing results predominantly address single-factor influences of temperature or corrosion on member behavior. For example, Talebi et al. [1] examined the high-temperature performance of cylindrical BRBs and reported hysteretic shapes comparable to those at ambient conditions, with core yielding remaining the dominant mechanism. In tests on BRBs with low-yield-point steel cores, Hu et al. [2] observed that exposure to 121–300 °C caused only minor reductions in plastic energy dissipation, while ductility and overall stability remained acceptable. While informative regarding environmental effects, these studies do not account for coupled temperature–humidity actions. Bridge-sector research [3] indicates that temperature cycling can alter the contact condition of frictional interfaces through thermal expansion and contraction, imposing additional LCF demand. This suggests that, under hygrothermal cycling, superposed variations in temperature and humidity may accelerate the evolution of interface friction characteristics and the deterioration of hysteretic parameters.

With respect to hygrothermal-related detailing, Wu et al. [4] reported that all-steel BRBs without an unbonded layer can preserve high hysteretic stability under LCF loading, but friction-induced local buckling markedly accelerates performance degradation. Rahaei et al. [5] and Ostovar & Hejazi [6] proposed PVC/FRP jackets or UHPFRC infill to enhance corrosion resistance and durability, while Ebanesar et al. [7] and Bae et al. [8] advocated EPS or PCM infill to improve environmental adaptability. Nevertheless, most of these studies were conducted at room temperature or without controlled humidity; quantitative characterization of material permeability, interfacial adhesion, and frictional evolution during wetting–drying cycling remains insufficient.

At the system level, fragility assessments conducted by Zaruma & Fahnestock [9] based on FEMA P-695 and life-cycle analyses coupling wind-induced fatigue with seismic actions [10] both show that when environmental degradation is considered, structural fragility curves and collapse capacities evolve significantly with service time. This implies that changes in BRB hysteretic parameters induced by hygrothermal cycling should be explicitly incorporated into structural analysis models to enable life-cycle seismic performance evaluation and optimization of maintenance strategies.

In summary, current research on BRBs under hygrothermal cycling presents the following gaps: (i) a lack of controlled, member-level experiments and parameter identification under coupled temperature–humidity actions; (ii) inadequate mechanistic quantification of interfacial frictional properties and the compression overstrength factor; (iii) incomplete understanding of the relationships among material degradation, interface behavior, and overall hysteretic performance before and after hygrothermal cycling; and (iv) a scarcity of system-level studies that feed degraded constitutive parameters into structural models for life-cycle seismic assessment.

Motivated by these gaps, this study focuses on Q235 grouted BRBs commonly used in practice. Controlled hygrothermal cycling tests are conducted to reveal the degradation laws of hysteretic performance; a modified Bouc–Wen degradation model is formulated and calibrated via a genetic algorithm; and, at the structural level, a benchmark steel frame is analyzed to quantify the impact of degradation paths on seismic response. Comparative evaluations of bracing schemes and sensitivity analyses are further performed to elucidate the chevron configuration's robustness to degradation-induced disturbances. The outcomes provide systematic theoretical support and practical guidance for material selection, detailing optimization, and life-cycle prediction of BRBs serving in hot–humid environments.

2. Experimental Program

2.1. Research Methodology

The steps for conducting this study is as follows: First, six grouted-type BRBs were subjected to 0, 24, 48, 72, 96, and 120 cycles of high-low temperature alternating hygrothermal tests, which were conducted in a dedicated test chamber. After the completion of the hygrothermal cycle tests, all specimens were uniformly subjected to surface cleaning and necessary protective treatments. Subsequently, quasi-static tests were performed using a 4000 kN damper test system, with displacement-controlled loading via a triangular wave at a frequency of 0.02 Hz. The loading protocol included 3 cycles each at displacement amplitudes of L/300, L/200, and L/150, 30 cycles at L/100 amplitude (to evaluate fatigue performance), and loading until failure at L/50 amplitude to verify the ultimate bearing capacity of the BRBs. Meanwhile, hysteretic curves and key mechanical performance parameters were collected synchronously.

Figure 1 shows the flowchart of the research methodology through which the objectives of this study were achieved.

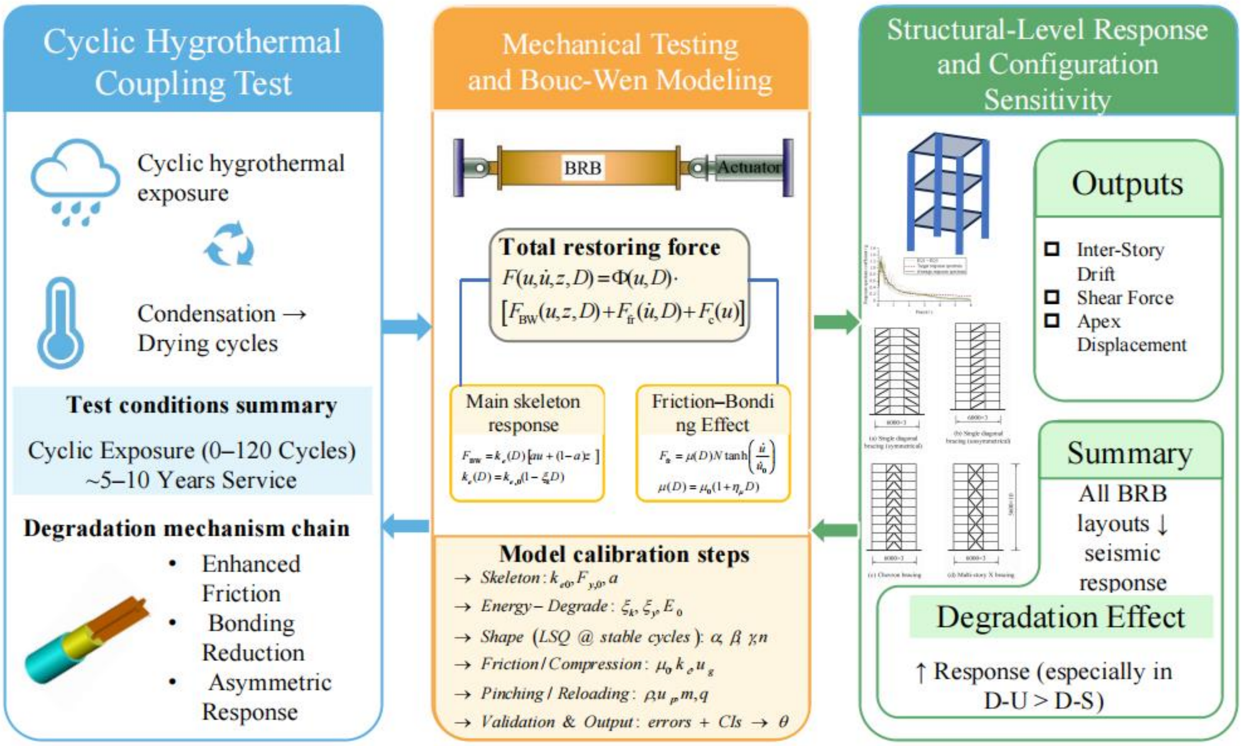

Figure 1. Flowchart of the research method

2.2. Specimen Design

To investigate the evolution of mechanical parameters of buckling-restrained braces (BRBs) under hygrothermal cycling, six grouted-type BRBs with identical geometry and properties were designed and fabricated. Each specimen employed a cruciform steel core plate restrained by a circular steel tube, with the annulus infilled by cement mortar. A 2 mm-thick unbonded layer was wrapped around the core within the restrained region. The configuration and dimensions are shown in Figure 2.

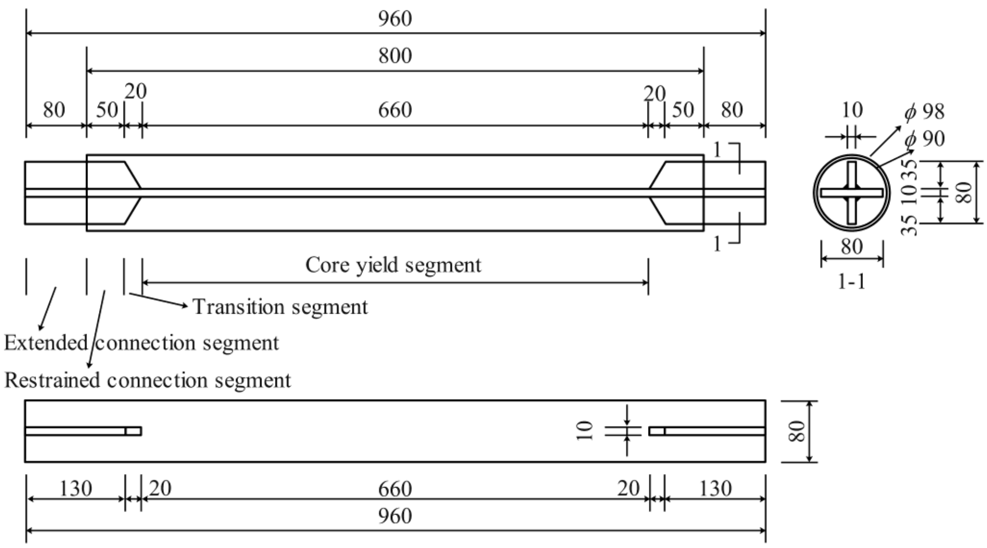

Figure 2. Geometric details of the BRB specimens (mm)

The core plates were made of Q235 low-carbon steel with a thickness of 10 mm, while the restraining tube was fabricated from Q345 low-alloy steel with a wall thickness of 8 mm. Material properties obtained from coupon tests are summarized in Table 1. End plates were welded to both ends of each specimen to facilitate connection to the loading apparatus.

Table 1. Material properties

Materials	f_y (MPa)	f_u (MPa)	ε_u (%)	E (GPa)	f_u/f_y
Q235	291.87	428.02	34.47	213.94	1.467
Q345	372.69	517.19	31.57	217.82	1.388

2.3. Hygrothermal Cycling Protocol

The experimental program comprised two stages. First, each specimen was subjected to alternating high–low temperature hygrothermal cycles to artificially simulate the hot–humid atmospheric environment encountered in service. Upon completion of the cycles, quasi-static tests were performed to evaluate mechanical degradation. For data grouping and traceability, specimens were labeled by cycle count as BRB0, BRB24, BRB48, BRB72, BRB96, and BRB120, corresponding to 0, 24, 48, 72, 96, and 120 cycles, respectively. After cycling, all specimens underwent unified surface cleaning and necessary protective treatment before the quasi-static loading stage. The hygrothermal cycling followed a typical daily pattern of heating–isothermal/humid–cooling/drying. The specific environmental parameters and dwell times were set with reference to the Chinese national standard GB/T 2423.34-2024 (Environmental testing-Part 2: Test methods-Test Z/AD: Combined temperature/humidity cyclic test). To verify the representativeness and reliability of the programmed parameters, coupon tests were carried out prior to the full-scale BRB tests on Q235 and Q345 steels from the same production heats. One coupon was sampled every 24 cycles to measure mass-loss rate. The results showed that, even at 120 cycles, only slight surface corrosion and limited property degradation occurred, indicating that the materials retained adequate integrity. Considering the service period and energy consumption of the test facility, 120 cycles was adopted as the upper bound for this study.

Figure 3 presents the relationship between the number of hygrothermal cycles and mass-loss rate and supports the need for clarification: the number of laboratory cycles prescribed herein is not directly equated to a specific "in-service exposure year." In durability research, a common approach is to use a per-cycle degradation metric and establish a correlation between accelerated indoor cycling and quality loss (e.g., mass loss) measured under natural atmospheric exposure. The computational scheme adopted in this paper is illustrated in Figure 3, and the test parameters are listed in Table 2.

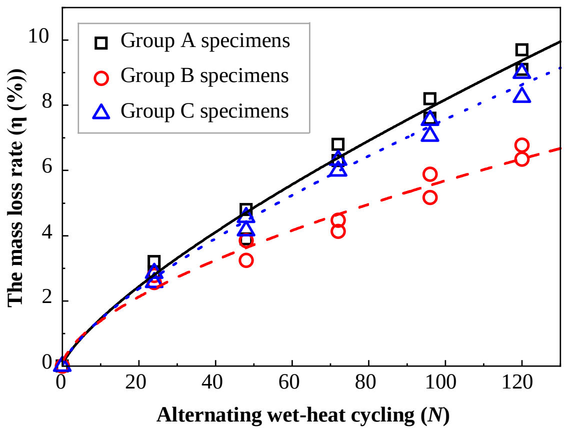

Figure 3. Mass loss versus cycle count (A: Q235; B: Q345; C: Q235 low-cycle fatigue)

Table 2. Parameters of high-low temperature alternating humidity test

Phase	Temperature (℃)	Relative humidity (℃)	Time (h)	
Heating period	25 ± 2 → 70 ± 2	≥ 95	2 ± 0.5	
High temperature and high humidity phase	65 ± 2	≥ 95	4	8 ± 1
Cooling phase	70 ± 2 → 25 ± 2	≥ 95	2 ± 0.5	

Based on the coupon results, the equivalent service time t_{eq} associated with N hygrothermal cycles can be approximated as

$$t_{\text{eq}}(N) = N \times \tau, \quad \tau \in [0.5, 1.0] \text{ month/cycle} \tag{1}$$

where τ is the experimentally inferred per-cycle degradation rate expressed in units of time. The range of τ depends on material grade, environmental severity, and detailing, and therefore is not used here to back-calculate an absolute service life.

Using this conversion, 120 cycles correspond roughly to 5–10 months of exposure in a hot–humid environment. To ensure stability and repeatability of the results and to avoid bias from reloading the same member, multiple independent specimens (rather than repeated loading of a single specimen) were adopted for each condition, and a unified loading protocol was used in the second stage after exposure. This strategy minimizes the influence of material scatter and fabrication tolerances and ensures comparability across specimen groups. Figure 4 illustrates the high-low temperature alternating humidity test, simulating cyclic environmental stress to evaluate material durability under fluctuating thermal and moisture conditions.

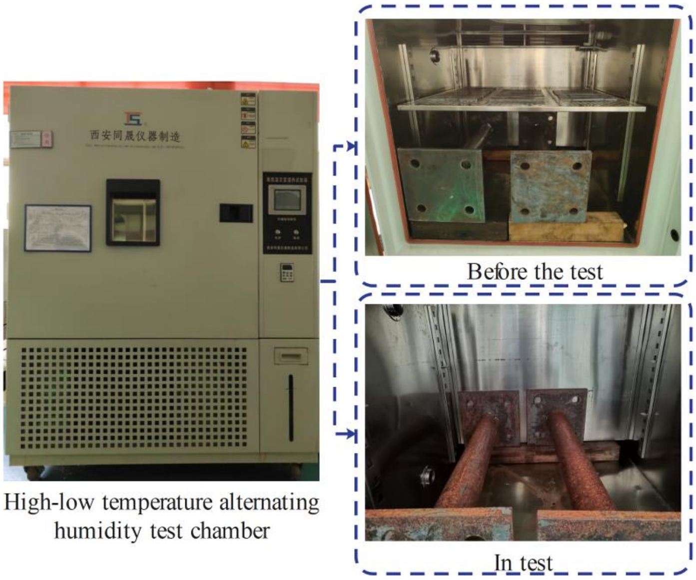

Figure 4. High-low temperature alternating humidity test

2.4. Hysteretic Performance Testing of the Brace

Hysteretic tests were conducted on a damper testing system with a rated capacity of 4000 kN. The setup comprised a loading end and a fixed end. End plates were welded to both ends of each brace and bolted to the machines bearing plates using high-strength bolts to ensure reliable anchorage. Axial load and displacement were acquired and recorded in real time by the testing system. To obtain the strain distribution of the restraining tube, electrical resistance strain gauges were installed at both ends and at midspan; at each section, four pairs of orthogonally oriented gauges were arranged uniformly. In addition, one pair of gauges was affixed to the protruding segments of the core plate at both the loading and fixed ends to monitor the stress state of the core, as shown in Figure 5.

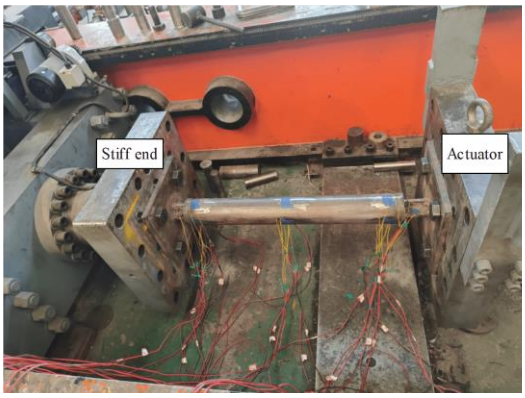

Figure 5. Pseudo-static test loading device

Displacement control was adopted with a triangular loading waveform at 0.02 Hz. Following the "Code for Seismic Design of Buildings" (GB 50011-2010) and the geometric relationship between brace deformation and interstory drift ratio, the elastoplastic drift limit of 1/50 for a single-diagonal brace layout corresponds to a maximum brace deformation of approximately $L/100$ (where L is the total brace length). The loading protocol consisted of three fully reversed cycles at displacement amplitudes of $L/300$, $L/200$, $L/150$, and $L/100$, followed by an additional 30 cycles at $L/100$ to evaluate the low-cycle fatigue performance of the BRB. To reflect the randomness and impulsive nature of seismic actions, larger displacement amplitudes were also applied to assess the ultimate load-carrying capacity. The complete loading scheme is summarized in Table 3.

Table 3. Pseudo-static test loading scheme

BRB	*L*/300	*L*/200	*L*/150	*L*/100	*L*/80	*L*/60	*L*/50
Loading cycles	3	3	3	30	3	3	Until fracture
Displacement (mm)	3.2	4.8	6.4	9.6	12	16	19.2

3. Results and Discussion

3.1. Observed Behavior

After three hygrothermal cycles, incipient corrosion appeared on the BRB surfaces and progressively intensified with increasing cycle count. At 72 cycles, local melting of the unbonded layer was observed, together with blister-like (bubbled) corrosion on the specimen surface; after 96 and 120 cycles these blisters further developed and subsequently ruptured with flaking and spalling. Representative surface damage at the end of cycling is shown in Figure 6.

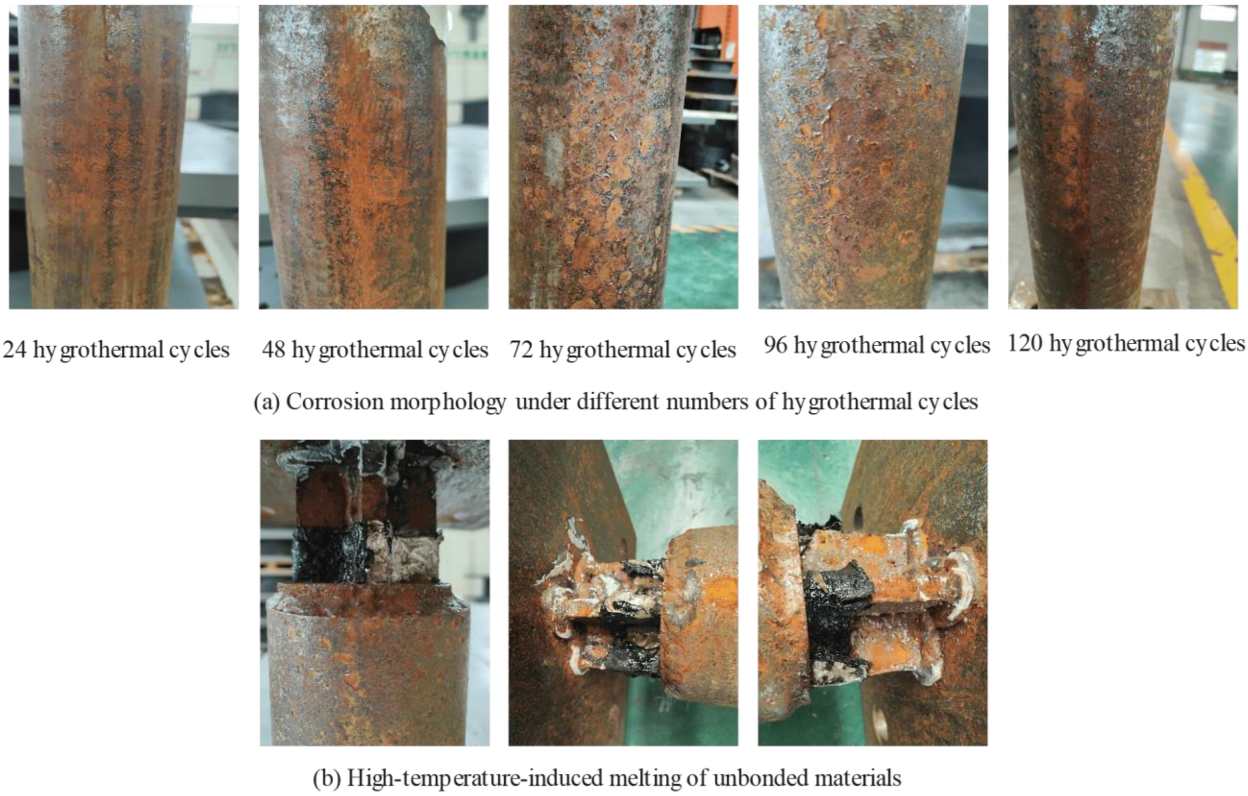

Figure 6. Surface morphology of specimens after hygrothermal cycles

Upon completion of the hygrothermal exposure, all specimens were surface-cleaned and prepared, strain gauges were affixed, and quasi-static loading tests were conducted. Tension was applied first, followed by compression. For displacement amplitudes smaller than $L/100$, no significant acoustic events were detected. When the amplitude reached $L/100$ and $L/50$, the final failure process was accompanied by pronounced dull snaps indicative of sudden damage. This phenomenon is plausibly attributed to intense bearing between the core plate and the mortar infill, causing local crushing of the mortar. Throughout testing, no specimen exhibited global instability, and no obvious warping or outward bulging of the restraining tube was observed. At the amplitude of $L/50$, all specimens failed by low-cycle fatigue, with fracture occurring within the yielded segment of the core plate. Specifically, specimens BRB0, BRB24, BRB48, BRB72, BRB96, and BRB120 failed at the 14th, 12th, 12th, 13th, 11th, and 11th loading cycles, respectively, with an abrupt loss of load-carrying capacity accompanied by distinct dull snaps.

In addition, post-test inspection revealed noticeable heating of the restraining tube surfaces for BRB48, BRB96, and BRB120, which is attributed to frictional heating generated between the core and the restraining assembly during compression. Crushed mortar extrusions were observed at the protruding segments of the core and on the floor beneath the lower end of each specimen; the exudate from BRB48 was predominantly in granular/fragmental form, whereas that from BRB96 and BRB120 appeared powdery (Figure 7).

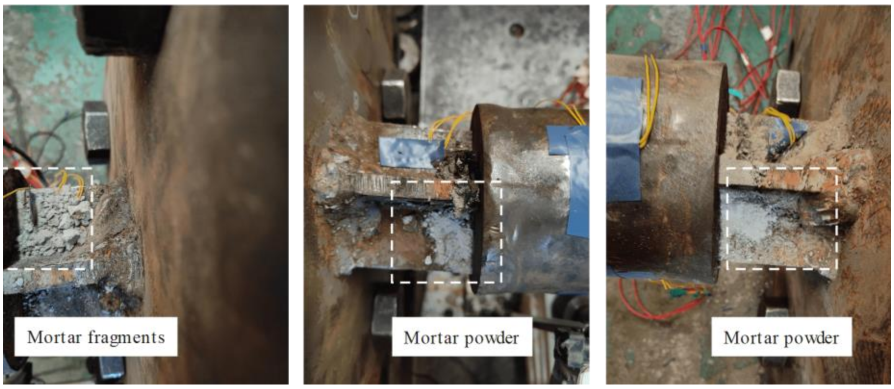

Figure 7. Failure modes of the filled mortar

3.2. Analysis of Test Results

(1) Hysteresis Loops and Backbone Curves

Figure 8 presents the hysteresis loops of the six BRB specimens. All loops are full and stable, with no evident pinching prior to failure; force–displacement responses at different amplitudes nearly coincide, and each specimen retained favorable energy-dissipation capacity after 30 fatigue cycles. The reference specimen BRB0 (without hygrothermal cycling) exhibited nearly symmetric tension–compression behavior. With increasing cycle count, the tensile resistance showed a slight decreasing trend, whereas the compressive resistance increased noticeably.

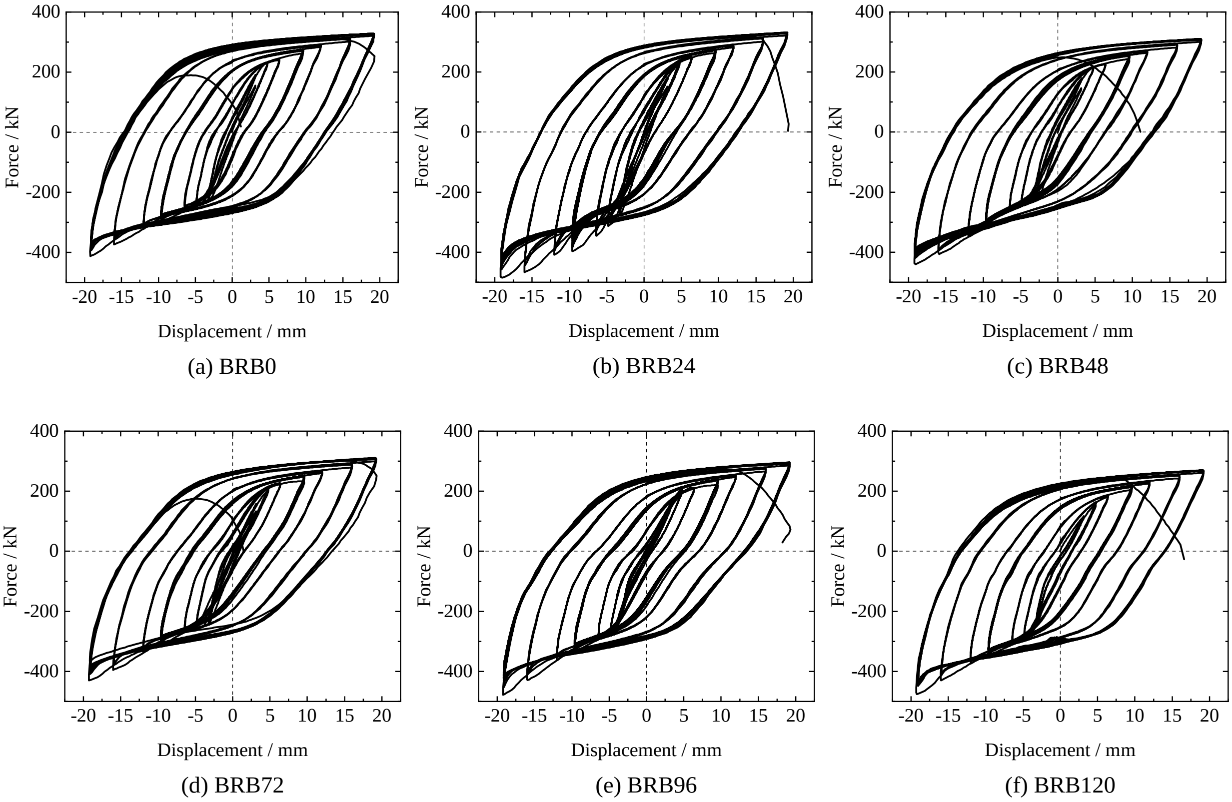

Figure 8. Hysteresis curve of the specimens

Table 4 summarizes the principal mechanical parameters. Hygrothermal cycling had a negligible effect on yield displacement; however, yield force, elastic stiffness, and cumulative hysteretic energy all decreased with cycle count. Relative to BRB0, the yield force after 24, 48, 72, 96, and 120 cycles decreased by 1.83%, 6.06%, 13.12%, 13.55%, and 30.68%, respectively, while the initial elastic stiffness declined by 6.42%, 11.03%, 16.30%, 17.06%, and 33.20%. The degradation is primarily attributed to: (i) accelerated corrosion of the steel core under hygrothermal cycling, which reduces strength and ductility; and (ii) moisture ingress at the core–restrainer interface driven by periodic temperature changes, which weakens adhesion between the unbonded layer and the core and promotes relative slip in tension. For BRB120, the larger reductions in yield force and stiffness are mainly associated with loosening of the clamping bolts under repeated tension–compression reversals.

Table 4. Mechanical property parameters of the specimens

Specimens	Δ_y (mm)	f_y (kN)	K (kN/mm)	K_{yt} (kN/mm)	K_{yc} (kN/mm)	N_{tmax} (kN)	N_{cmax} (kN)	E (kJ)
BRB0	4.49	230.02	51.23	7.94	9.25	327.85	-413.48	421.25
BRB24	4.71	225.82	47.94	8.74	12.99	331.54	-486.15	371.70
BRB48	4.74	216.07	45.58	7.52	14.42	310.13	-440.54	354.28
BRB72	4.66	199.84	42.88	8.98	11.54	311.05	-430.66	367.90
BRB96	4.68	198.86	42.49	6.87	10.81	295.78	-479.07	342.56
BRB120	4.66	159.45	34.22	9.48	10.48	269.63	-476.97	349.07

The compressive post-yield stiffness exhibited a rise–then–fall pattern: the value for BRB0 was 9.25 kN/mm, increased to a peak of 14.42 kN/mm after 48 cycles (55.86% higher than BRB0), and then decreased gradually to 10.48 kN/mm after 120 cycles, still 13.31% above BRB0. The initial increase can be ascribed to further curing/crystallization of the mortar that enhances restraining stiffness, together with strain hardening of the steel; at higher cycle counts, microcracking and porosity in the mortar develop, steel corrosion intensifies, and higher-order local buckling waves induce local crushing of the mortar, weakening the restraint and reducing stiffness. The slight early-stage increase in compressive stiffness likely reflects the combined effects of late-age mortar hydration strength gain and initial strain hardening of the steel, with the former being more influential, whereas strain hardening becomes more pronounced in mid-to-late hysteresis.

The degradation of ultimate tensile capacity mirrors that of the yield force, decreasing with cycle count for the same reasons (steel property loss and reduced interfacial adhesion). By contrast, the ultimate compressive capacity of the cycled specimens generally exceeded that of BRB0 by 6.54%–17.58%, albeit without a clear monotonic trend. This behavior may be related to aging-induced cracking of the unbonded layer, increased friction between the core and the restraining assembly [11] , and frictional amplification associated with mortar crushing under large displacements. Quantifying the relative contributions of these factors to the observed increase in compressive capacity warrants further study. In addition, the total hysteretic energy of the cycled specimens was 11.76%–18.68% lower than that of BRB0, indicating that hot–humid exposure also deteriorates cumulative energy-dissipation capacity.

Backbone curves constructed from the maximum tensile and compressive points at each displacement amplitude are shown in Figure 9. With increasing displacement amplitude, both tensile and compressive resistances increase; however, greater hygrothermal cycle counts reduce tensile resistance while enhancing compressive resistance. These results suggest that, under low-to-moderate hygrothermal cycling, the adverse effects on interface adhesion of the core–restrainer unit and on the mortar's mechanical properties outweigh the direct effects of steel corrosion, thereby weakening composite action and adversely affecting overall brace performance [12, 13].

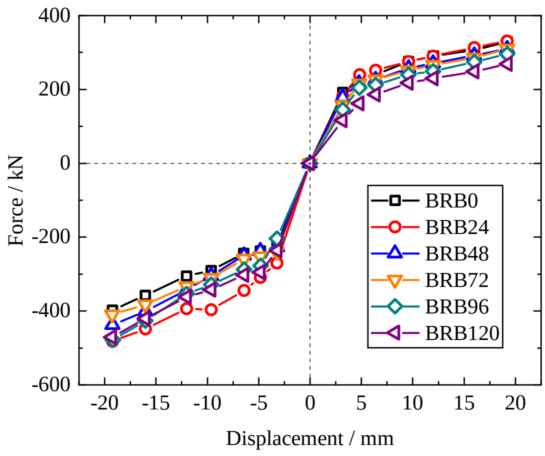

Figure 9. Skeleton curve of specimens

It should be noted that the degradation of concrete or mortar is influenced not only by hygrothermal cycling but also by long-term actions such as creep and carbonation. Nevertheless, this study focuses on the mechanisms by which hot–humid environments affect mechanical performance; the synergistic degradation induced by other factors-including creep and carbonation-will be investigated in future work.

Δ_y and F_y denote the measured yield displacement and yield force of the brace, respectively; K represents the elastic stiffness of the brace; K_{yt} and K_{yc} stand for the post-yield stiffness under tension and compression of the brace, respectively; N_{tmax} and N_{cmax} refer to the ultimate tensile bearing capacity and ultimate compressive bearing capacity of the brace, respectively; E is the total hysteretic energy dissipation of the brace.

(2) Equivalent Viscous Damping Ratio

The equivalent viscous damping ratio is a key index for evaluating the energy-dissipation capacity of BRBs. Considering the tension–compression asymmetry, the ratio was computed separately for the tensile and compressive segments using the last stabilized loop at each displacement amplitude. The calculation is given by Equations 2 and 3 and illustrated in Figure 10.

$$\zeta_{\mathrm{eq}}^{+} = \frac{1}{2\pi}\frac{S_{AEFA}}{S_{\Delta AOB}} \quad (2)$$

$$\zeta_{\mathrm{eq}}^{-} = \frac{1}{2\pi}\frac{S_{CEFC}}{S_{\Delta COD}} \quad (3)$$

where S_{AEFA} and S_{CEFC} denote the areas enclosed by the hysteresis curve in the tensile and compressive segments, respectively, and $S_{\Delta AOB}$ and $S_{\Delta COD}$ are the areas of the corresponding reference triangles.

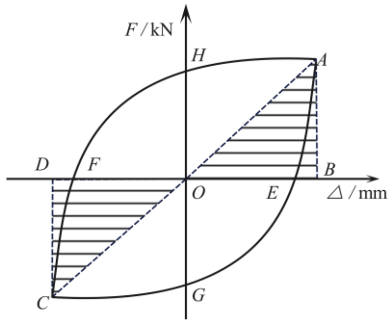

Figure 10. Schematic diagram for calculation of equivalent viscous damping ratio

Figure 11 shows the evolution of the equivalent damping ratios for each BRB with increasing displacement amplitude. Overall, the ratios increase with amplitude. Except for BRB0, all specimens exhibit larger tensile than compressive equivalent damping ratios, and the difference enlarges as the amplitude grows. At the maximum amplitude, the tensile ratios ζ_{eq}^{+} for BRB0, BRB24, BRB48, BRB72, BRB96, and BRB120 are 0.361, 0.353, 0.360, 0.361, 0.380, and 0.429, respectively; the corresponding compressive ratios ζ_{eq}^{-} are 0.352, 0.324, 0.333, 0.327, 0.304, and 0.297. These results indicate that hygrothermal cycling has a limited effect on ζ_{eq}^{+}, whereas ζ_{eq}^{-} decreases markedly with the number of cycles—from an initial 0.352 to 0.297 (a reduction of 15.63%).

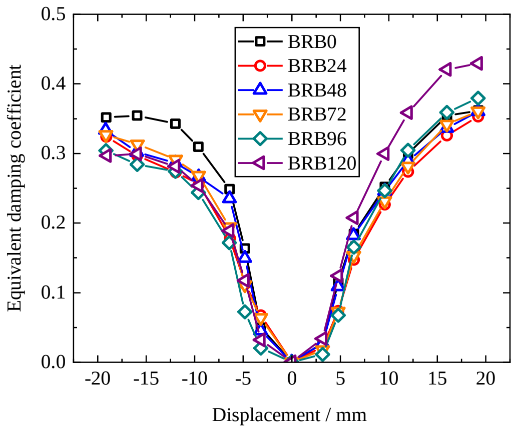

Figure 11. Equivalent viscous damping ratios under different loading displacements

Two primary mechanisms underlie the reduction in ζ_{eq}^{-}. First, at large compressive displacements, the enhanced Poisson effect and increased friction between the core plate and the restraining member cause warping near the compressive extremum of the loop, so the load cell underestimates the true axial force. Second, hygrothermal cycling degrades and may crack the unbonded layer, making axial friction between the core and the restrainer difficult to release; this provides additional load-bearing contribution during compression, suppresses energy-dissipation enhancement, and thus lowers the equivalent damping ratio.

Moreover, in the late loading stage, BRB120 shows a faster increase in ζ_{eq}^{+} than the other specimens. This is mainly attributed to a slight clearance between the clamping bolts and the end plate, which renders the actual tensile displacement smaller than the prescribed control displacement, thereby restraining further growth of axial force and yielding a comparatively higher value of the equivalent damping ratio in the calculation.

(3) Tension–Compression Asymmetry

To quantify the post-cycling increase in compressive resistance relative to tensile resistance, the tension–compression asymmetry factor β is introduced:

$$\beta = \frac{N_{cmax}}{N_{tmax}} \tag{4}$$

where β denotes the asymmetry factor, and N_{cmax} and N_{tmax} are the ultimate compressive and tensile strengths, respectively, at the same displacement amplitude.

According to the "Technical Specification for Application of Buckling-Restrained Braces" (T/CECS 817-2021), the limit for the single-cycle tension–compression nonuniformity coefficient is 1.30. On this basis, compliance and amplitude dependence were evaluated.

To examine the effect of displacement amplitude on β, statistics were compiled for each specimen at amplitudes from $L/300$ to $L/50$ (Figure 12). The results show that when the amplitude is below $L/100$, β for most specimens decreases slightly or remains approximately constant with increasing amplitude. As the amplitude approaches $L/100$, β exhibits a pronounced jump and reaches a peak near $L/50$. This "platform-to-jump" evolution is more evident in specimens subjected to a larger number of hygrothermal cycles.

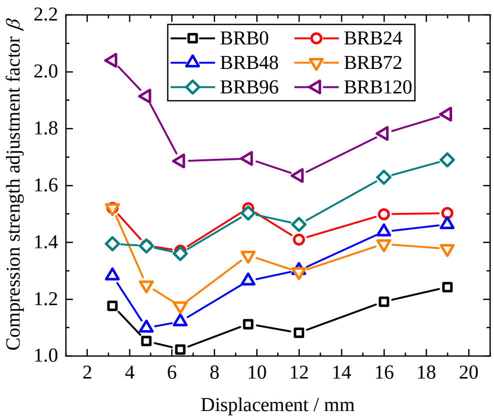

Figure 12. The compression strength adjustment factors of specimens under different displacement amplitudes

The terminal segment of the compressive branch displays through-thickness local stiffness and a high peak strength, attributable to the coupled action of three mechanisms:

i. Aging and cracking of the unbonded layer increase the friction coefficient between the core plate and the restraining unit; simultaneously, the normal contact pressure in compression grows with displacement and cumulative energy input;

ii. Late-age hydration and crystallization of the mortar locally enhance the restraining stiffness, but pulverization under large compressive strains leads to a sequential "stiffening→degradation" process;

iii. End-plate bolts and a curved-axis effect induce axial–bending coupling within the plastic hinge region, thereby elevating the compressive peak.

Compliance with $\beta \leq 1.30$. Referencing Figure 12, at $L/100$ the baseline specimen BRB0 has $\beta = 1.24$, satisfying the code limit. After hygrothermal cycling, the β values at $L/100$ for BRB24, BRB48, BRB72, BRB96, and BRB120 are 1.25, 1.35, 1.35, 1.59, and 1.62, respectively; at $L/50$ they further increase to 1.34, 1.60, 1.75, 1.82, and 1.83. Overall, β increases with displacement amplitude and with the number of hygrothermal cycles, with the jump becoming more pronounced at higher cycle counts. This phenomenon is likely related to residual deformation and cumulative damage, and it suggests the need for asymmetric detailing requirements in brace and system-level seismic design when β -based criteria are employed [14, 15].

(4) Cumulative Plastic Deformation

The cumulative plastic ductility coefficient (CPD) is defined as the ratio of the total plastic deformation after yielding to the yield displacement, and it characterizes the plastic deformation capacity of the brace. It is computed as

$$\text{CPD} = \sum_{i=1}^{n} \left[2\left(|\Delta_{i,max}| + |\Delta_{i,min}|\right)/\Delta_y - 4\right] \tag{5}$$

where $\Delta_{i,max}$ and $\Delta_{i,min}$ are, respectively, the maximum tensile and maximum compressive deformations of the i-th hysteresis loop, and Δ_y is the yield displacement.

Using Equation 5, the CPD values for BRB0, BRB24, BRB48, BRB72, BRB96, and BRB120 are 373.66, 309.83, 304.90, 338.62, 313.08, and 301.94, respectively. Relative to BRB0, these represent reductions of 17.08%, 18.40%, 9.38%, 16.21%, and 19.19%. The ANSI/AISC 341-05 provisions specify that the cumulative plastic ductility coefficient of metallic yielding braces shall not be less than 200; all specimens satisfied this requirement. Thus, even after up to 120 hygrothermal cycles the braces retained adequate plastic deformability. Nevertheless, failure of the unbonded layer induced by cycling, a reduction in the clamping action of the restraining unit on the core, and frictional heating under compression collectively led to a marked decrease in CPD.

(5) Energy-Dissipation Stability

According to JGJ 297-2013 ("Technical Specification for Seismic Energy Dissipation in Buildings"), after 30 cycles of low-cycle fatigue loading, the stability indices of a metallic damper should fall within ±5% of their mean values over all cycles. Following the specification, we evaluated for each cycle the ratios between: (i) the maximum (minimum) damper force and the mean of the maximum (minimum) forces over all cycles, denoted $\gamma_{F,max}$ and $\gamma_{F,min}$; (ii) the damper force at zero displacement and its mean over all cycles, denoted $\gamma_{F0,max}$ and $\gamma_{F0,min}$; and (iii) the zero-force displacement and its mean over all cycles, denoted $\gamma_{\Delta 0,max}$ and $\gamma_{\Delta 0,min}$. For each index, the minimum value and the mean were used for assessment.

Within the present tests, the fluctuations of all indices were small and satisfied the ±5% criterion, indicating stable performance and satisfactory low-cycle fatigue resistance. As the number of cycles increased, $\gamma_{F,max}$ exhibited a "rise–then–stabilize" trend, revealing evident cyclic hardening; $\gamma_{F,min}$, $\gamma_{\Delta 0,max}$, and $\gamma_{\Delta 0,min}$ decreased slightly in the early cycles and then stabilized, consistent with initial slip of the unbonded layer and the progressive stabilization of frictional contact. The displacement amplitude at the $L/100$ fatigue segment was only 9.56 mm, and no specimen failed during the prescribed $L/100$ cycling (fracture occurred subsequently under the larger $L/50$ amplitude). Consequently, the influence of hygrothermal cycling on the remaining stability indices is relatively minor and is not discussed further here [16, 17] (Figure 13).

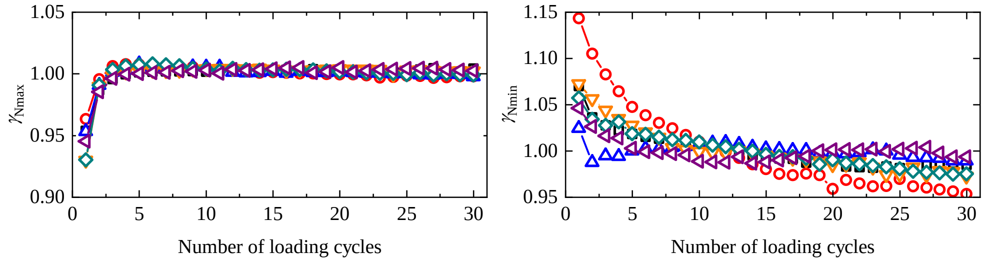

(a) Maximum damping force (b) Minimum damping force

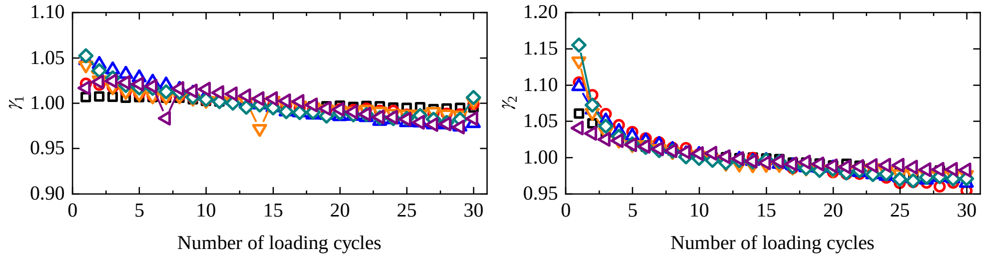

(c) Maximum damping force at zero displacement (d) Minimum damping force at zero displacem

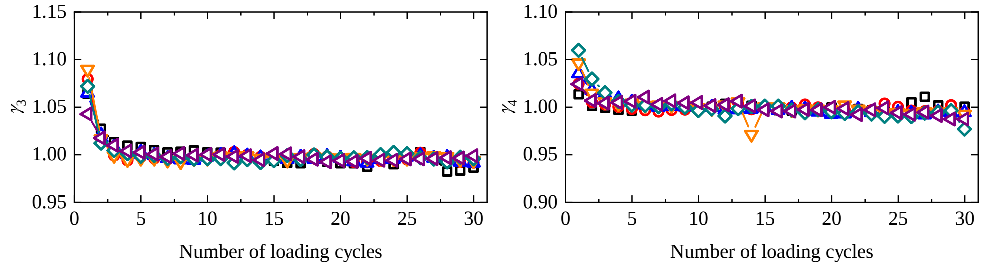

(e) Maximum displacement at zero force (f) Minimum displacement at zero force

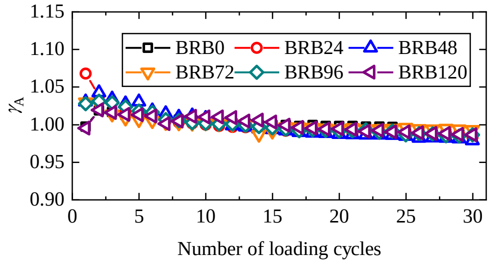

(g) Area of hysteresis curve

Figure 13. The fatigue performance parameters of the specimens

4. Constitutive Modeling and Parameter Identification

Based on the test results, hygrothermal cycling causes pronounced degradation in BRB performance, manifested primarily by reductions in yield force, ultimate tensile strength, and elastic stiffness, together with an intensified tension–compression asymmetry driven by increased axial friction. Classical restoring- force models include bilinear, multilinear, and Bouc–Wen formulations. Among these, the Bouc–Wen model is widely adopted because it can reproduce complex hysteretic features such as smooth loop evolution, kinked corners, slip and pinching, post- yield stiffness deterioration, amplitude-dependent degradation, and strength loss (Figure 14).

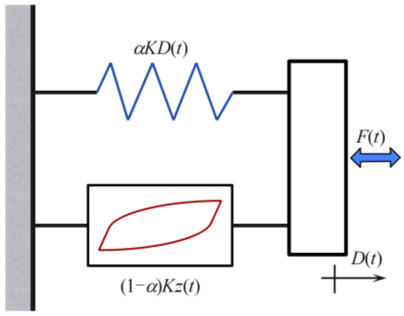

Figure 14. Physical significance of the Bouc-Wen model

To capture the observed behaviors, a coupled degradation–friction Bouc–Wen model is proposed. On the Bouc–Wen backbone, we introduce a biased memory mechanism, an evolutionary viscous–friction branch, a unilateral contact stiffness to describe gap closure, and an amplitude–damage–dependent control factor to represent pinching. The composite restoring force is expressed as:

$$F(u, \dot{u}, z, D) = F_{BW}(u, z, D) + F_{Fr}(\dot{u}, D) + F_c(u) + \Phi(u, D) \tag{6}$$

where u and $\dot{u}$ are the displacement and velocity of the brace, z is the internal hysteretic variable, and D is a cumulative degradation (damage) index. The term F_{BW} denotes the main Bouc–Wen restoring component; F_{Fr} represents friction; F_c accounts for unilateral contact in compression; and Φ is a pinching control term that modulates the loop opening.

4.1. Degradation–Type Bouc–Wen Backbone

The backbone response is described by a degraded Bouc–Wen model:

$$F_{BW} = k_s(D)[\alpha u + (1-\alpha)z], \quad k_s(D) = k_s^0(1-\xi_k D) \tag{7}$$

where k_s^0 is the initial stiffness, $k_s(D)$ is the degraded stiffness, ξ_k is the stiffness degradation coefficient, and α is the post-yield stiffness distribution factor. The evolution of the internal variable z follows

$$\dot{z} = a\dot{u} - \beta|\dot{u}||z|^{n-1}z - \gamma\dot{u}|z|^n \tag{8}$$

where; a, β, γ, n are Bouc–Wen shape parameters controlling loop angle, width, and stress–recovery characteristics.

4.2. Frictional Branch and Contact Effect

Accounting for interface slip and running-in wear, the frictional contribution is modeled by a smooth Coulomb law:

$$F_{Fr} = \mu(D)N\, tanh\left(\frac{\dot{u}}{u_0}\right), \quad \mu(D) = \mu_0(1+\eta_D D) \tag{9}$$

where $\mu(D)$ is the damage-enhanced friction coefficient, N is the normal contact pressure, u_0 is a velocity scale, μ_0 is the base friction coefficient, and η_D is a friction–damage coupling parameter.

During compression, concurrent action of end stops and constructional contact produces a rapid stiffness increase. A unilateral contact spring is therefore introduced:

$$F_c(u) = k_c\langle -u + u_g\rangle_+ \tag{10}$$

where $\langle\cdot\rangle_+$ denotes the positive part, u_g is the initial gap, and k_c is the contact stiffness; this term effectively captures the nonlinear stiffening during gap closure.

To further characterize progressive loop closure and reopening at small amplitudes, an amplitude–damage control factor is adopted:

$$\Phi(u, D) = 1 - \rho\frac{D^q}{1 + (|u|/u_p)^m} \tag{11}$$

where ρ, u_p, m, q control the severity of pinching, the amplitude sensitivity, and the coupling strength with degradation, enabling realistic pinching behavior at low displacement levels.

The effective damage index D evolves with dissipated energy as:

$$D(k) = 1 - exp\left(-\frac{\sum_{i=1}^{k}\Delta E_i}{E_0}\right), \quad \Delta E_i = \oint_i F\, du \tag{12}$$

where ΔE_i is the energy dissipated in the i-th stabilized loop and E_0 is the energy scale for degradation onset.

4.3. Stepwise Parameter Identification

To ensure engineering identifiability of the model parameters, a stagewise calibration workflow based on hysteresis data is established:

1. Backbone extraction: From the backbone slope and yield point, obtain the initial stiffness k_s^0, yield strength F_y^0, and the stiffness distribution factor α.
2. Degradation fitting: Using energy integrals of stabilized loops and the observed degradation trends, calibrate the degradation parameters ξ_k, ξ_z (if used for z–degradation), and the energy scale E_0.
3. Bouc–Wen shape: Under high-amplitude stabilized cycles, identify a, β, γ, n via least squares to match loop angle and curvature.
4. Friction and contact: From the low-velocity plateau and the amplitude-dependent increase of compressive stiffness, estimate μ_0, k_c, and u_g (together with η_D if applicable).
5. Pinching control: From the measured evolution of loop opening with amplitude, fit the pinching parameters ρ, u_p, m, q.

This coupled degradation–friction Bouc–Wen formulation reproduces the experimentally observed tension–compression asymmetry, strength and stiffness deterioration, partial stiffness recovery, and amplitude-dependent pinching, while retaining good numerical robustness and extensibility for structural analysis.

Figure 15 demonstrates the alignment between experimental data and model predictions, while Table 5 presents the identified parameters of the improved Bouc-Wen model that underpin this correlation.

Table 5. Parameter identification results of the improved Bouc-Wen model

Parameters	α	K	D_y	η	λ	υ	ρ	β	γ
BRB0	0.029	56	4.98	1.08	1.25	1.05	1.101	0	1
BRB24	0.025	54	4.95	1.13	1.38	1.21	1.184	-0.45	1.45
BRB48	0.021	51	4.88	1.14	1.38	1.25	1.198	-0.35	1.35
BRB72	0.021	51	4.86	1.14	1.38	1.28	1.198	-0.35	1.35
BRB96	0.018	48	4.81	1.18	1.38	1.42	1.257	-0.35	1.35
BRB120	0.011	46	4.68	1.18	1.38	1.51	1.257	-0.65	1.65

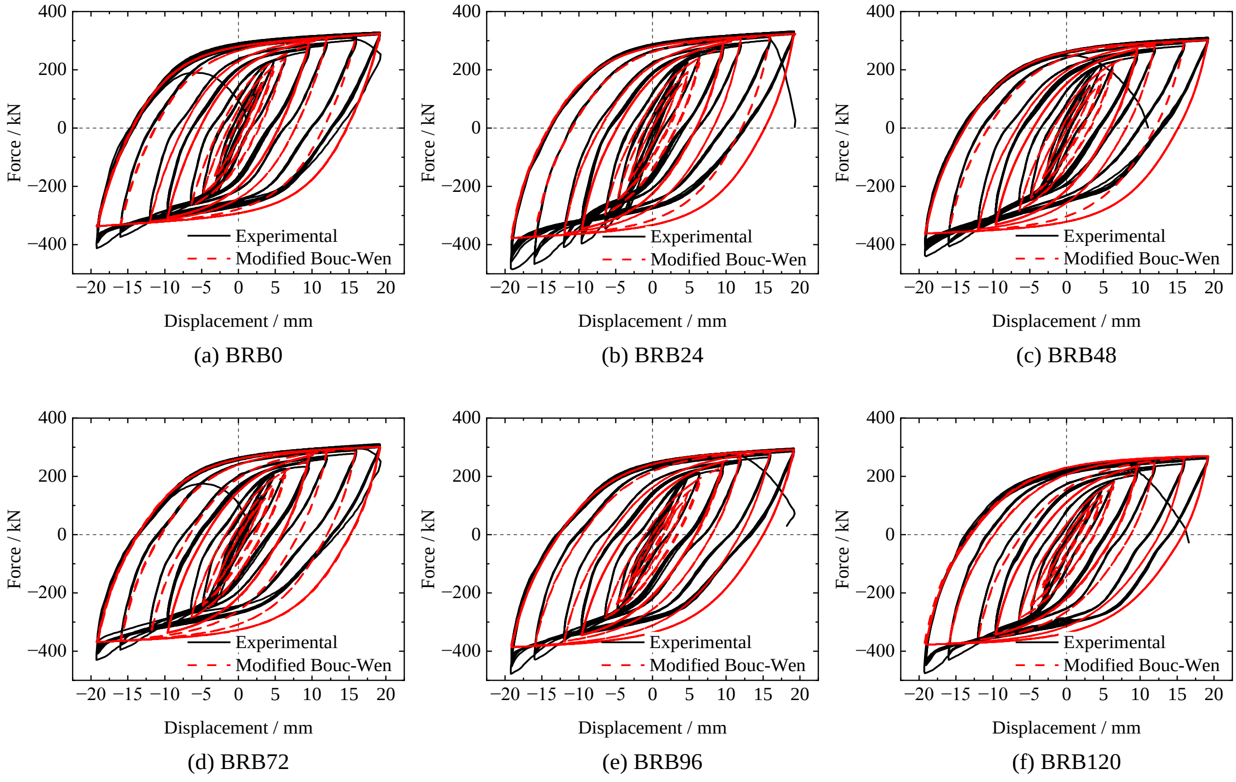

Figure 15. Comparison between test results and fitting results

5. Case Study

5.1. Project Description

Hygrothermal cycling reduces the elastic stiffness and tensile capacity of BRBs but markedly increases their compressive capacity and post-yield compressive stiffness, thereby amplifying tension–compression asymmetry. When such braces are incorporated into a dual lateral-force-resisting system with a moment frame, it is necessary to quantify the influence of brace performance degradation on the global seismic response [18-20].

A ten-story planar reinforced-concrete (RC) moment frame from an actual project is used as the prototype. Story height is 4.5 m; the frame has three bays, each 6 m in span. Three BRB layouts are considered for seismic retrofit/design of the frame: single-diagonal, chevron (inverted-V), and multi-story X-braced schemes (see Figure 16). The gravity loads are 36 kN/m (dead) and 18 kN/m (live). The seismic fortification intensity is 8 (design basic acceleration 0.20 g); the site is Class II with Seismic Group II, and the site characteristic period is 0.40 s. Beams and columns use C30 concrete; both longitudinal and transverse reinforcement are HRB400, with a nominal concrete cover of 20 mm for beams and columns.

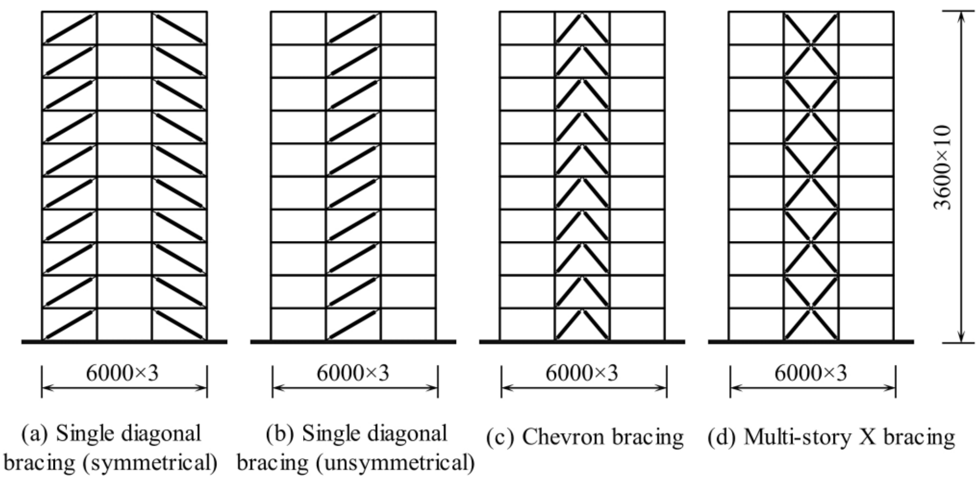

Figure 16. Schematic diagram of the calculation model

A preliminary design was first conducted following conventional procedures. Rectangular RC columns were adopted: 600 mm × 600 mm with 8C25 longitudinal bars for Stories 1–5, and 450 mm × 450 mm with 8C22 bars for Stories 6–10. Rectangular RC beams were 250 mm × 450 mm, with 3C25 bottom longitudinal bars and 2C16 top longitudinal bars; all beam and column stirrups were C8@100/200. After completing the preliminary frame design, the required cross-sectional area of a single BRB in the analysis model was determined from the target frame-to-brace lateral stiffness ratio; the values used are listed in Table 6.

Table 6. Cross-sectional area of the BRB core

Layer number	Cross-sectional area /mm^2			
	Single diagonal bracing (symmetrical)	Single diagonal bracing (unsymmetrical)	Chevron bracing	Multi-story X bracing
1	1356	2712	3242	3242
2	606	1212	1450	727
3	606	1212	1450	1454
4	606	1212	1450	727
5	606	1212	1450	1454
6	526	1052	1258	727
7	526	1052	1258	1454
8	526	1052	1258	727
9	421	842	1006	1010
10	421	842	1006	505

5.2. Selection of Ground Motions

Five strong- motion records were obtained from the Pacific Earthquake Engineering Research (PEER) Center database. Each record was amplitude-scaled to the maximum considered earthquake (MCE) level in terms of peak ground acceleration (PGA) and then used as input for nonlinear time-history analyses. The response spectra of the scaled records, together with the code spectrum, are shown in Figure 17. Detailed information on the selected motions is provided in Table 7.

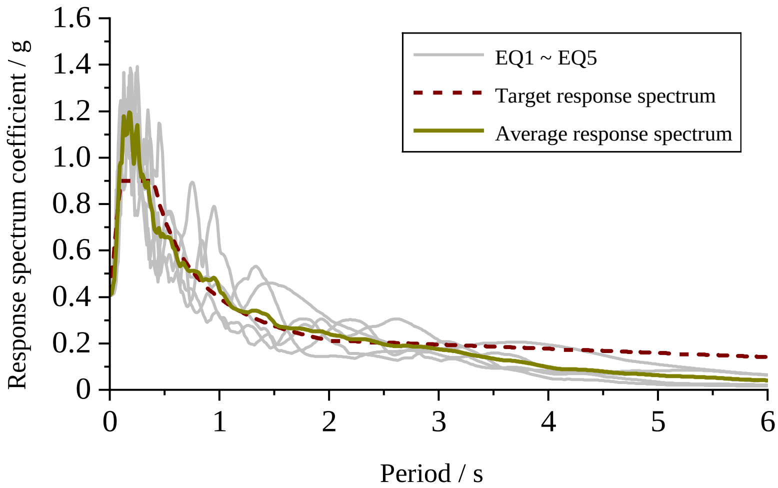

Figure 17. Comparison between seismic wave response spectrum and code spectrum

Table 7. Information of seismic waves selected for dynamic time-history analysis

Number	Name of earthquake	Site of record	Year	Magnitude	Amplitude modulation factor
EQ1	Big Bear-01	Phelan - Wilson Ranch	1992	6.46	9.14
EQ2	Chi-Chi_Taiwan-05	CHY107	1999	6.2	7.197
EQ3	Chi-Chi_Taiwan-05	CHY039	1999	6.2	6.08
EQ4	San Fernando	LA - Hollywood Stor FF	1971	6.61	1.802
EQ5	Northridge-01	Phelan - Wilson Ranch	1994	6.69	8.586

5.3. Seismic Response Analysis

Using the five MCE-level records in Table 7 as input, the hysteretic behavior of BRBs was simulated with the modified Bouc–Wen model proposed earlier. A systematic parametric study was performed to evaluate how different degrees of BRB performance degradation affect the global seismic response for various bracing layouts. In the notation adopted herein, BRBF denotes a buckling-restrained braced frame; the numerical suffix indicates the number of hygrothermal cycles, and the final letter indicates the layout: “ds” = single-diagonal symmetric (D-S), “du” = single-diagonal asymmetric (D-U), “c” = chevron (inverted-V), and “x” = multi-story X-braced (Multi-X). For example, BRBF120-c denotes a chevron-braced frame incorporating BRB degradation after 120 hygrothermal cycles

Figures 18 to 20 plot the interstory drift ratios, story shears, and roof displacements, respectively, for the different layouts. Relative to the bare frame, all four BRB configurations markedly improve seismic performance: the maximum interstory drift ratio is reduced by 42.22%–51.82%, the maximum story shear by 53.53%–77.86%, and the roof displacement by 36.84%–47.90%. Among the schemes, the chevron layout provides the greatest improvements for all three indices and yields more uniform distributions of drift and story shear; the single-diagonal asymmetric layout is comparatively less effective. Mechanistically, the mid-span chevron node distributes vertical forces to the two braces, enabling dual-member sharing of story shear. This enhances energy-dissipation efficiency and mitigates local stress concentrations at the node, thereby suppressing the amplification of global displacements by local deformations. In contrast, a single-diagonal member has a larger slenderness ratio and a single force-transfer path; under strong shaking it is prone to excessive deformation and failure, and axial deformation contributes a larger portion of the interstory drift.

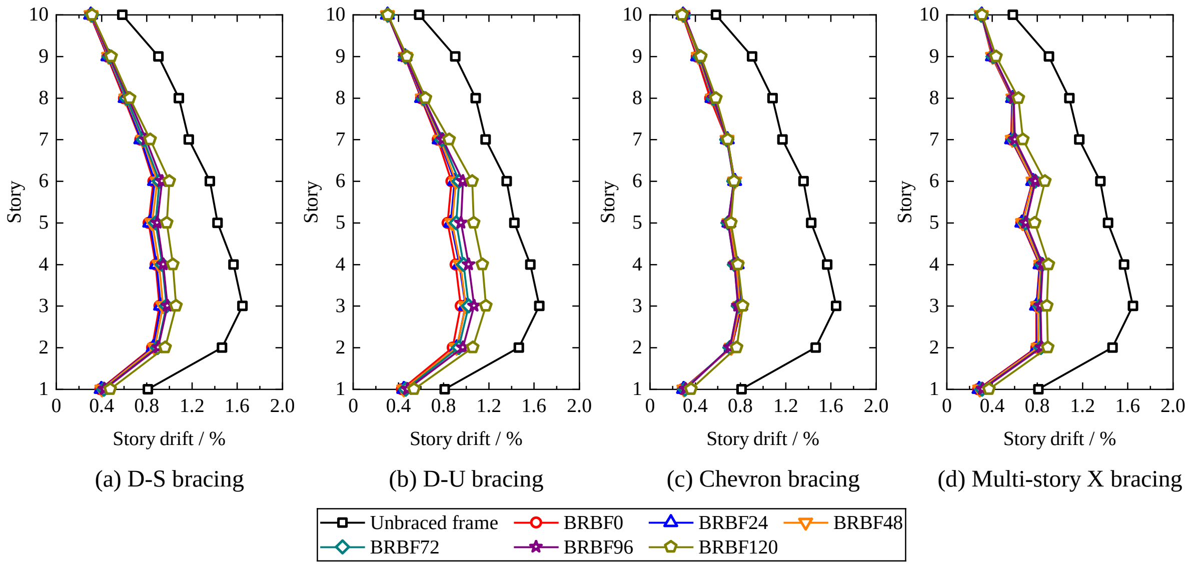

Figure 18. Comparison of story drift ratios

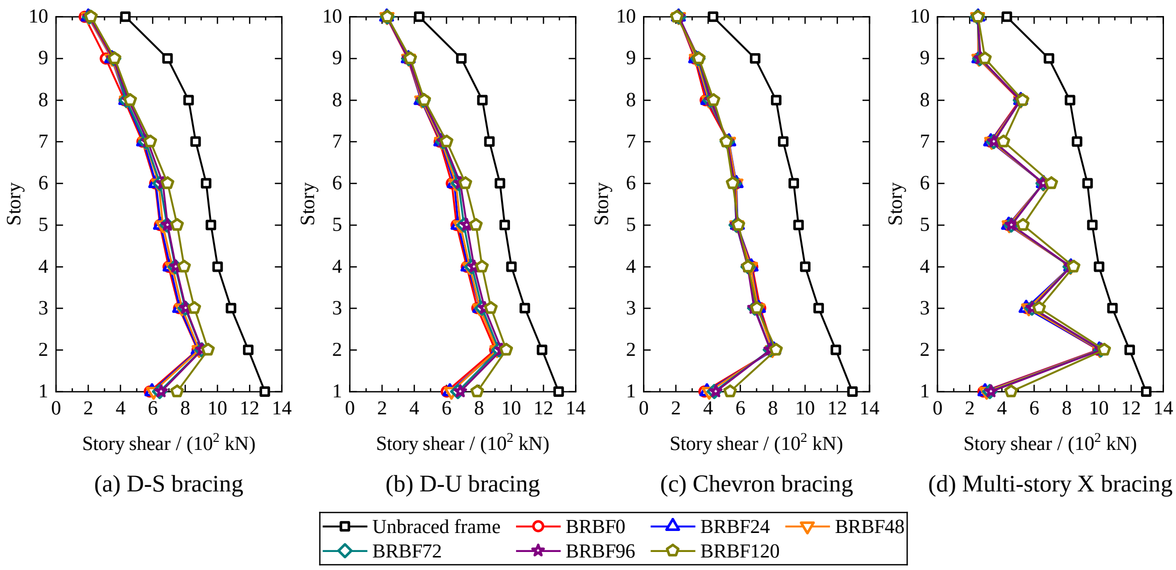

Figure 19. Comparison of story shear

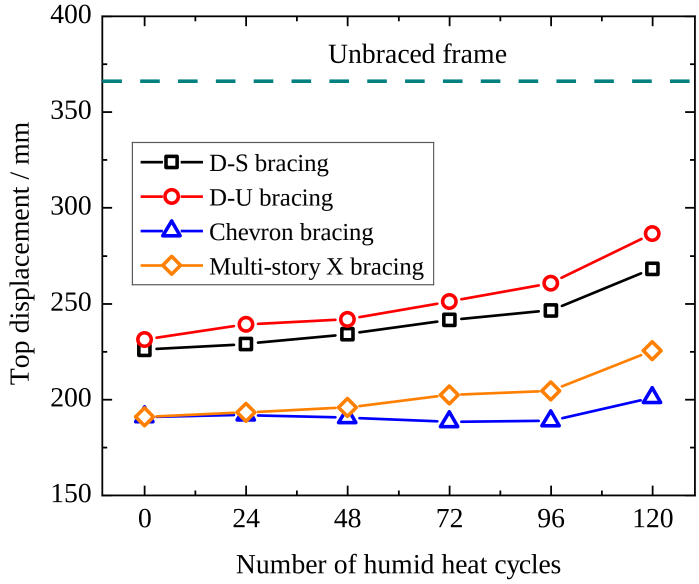

Figure 20. Comparison of top displacements

Compared with BRBF0 (no degradation), incorporating BRB degradation significantly amplifies structural responses. For the 120-cycle case, the increases in maximum interstory drift ratio are 16.22%, 23.67%, 1.14%, and 11.87% for BRBF120-ds, BRBF120-du, BRBF120-c, and BRBF120-x, respectively; the corresponding increases in maximum story shear are 7.51%, 7.76%, 2.02%, and 3.64%; and the increases in roof displacement are 18.72%, 23.96%, 5.36%, and 18.10%. Under the same ground motions, structural responses grow monotonically with the degree of degradation. Although degradation does not change the location of the weak story, the response at that story is more sensitive to degradation. At the same degradation level, the chevron and multi-X layouts most effectively attenuate degradation-induced amplifications, whereas the single-diagonal asymmetric layout is the most sensitive because degradation strengthens tension–compression asymmetry, enlarging the disparity between lateral stiffness and energy-dissipation in tension and compression.

Across the range of hygrothermal cycles, the four layouts (D-S, D-U, Chevron, and Multi-X) exhibit distinct trends in roof displacement (Figure 20). These differences arise not only from geometric symmetry but also from inherent redundancy and load-path characteristics. The D-S layout relies on a single diagonal load path; as the asymmetry factor β increases, compressive axial forces concentrate at the corner joint, promoting additional torque and second-order (P–Δ) effects. The D-U layout, being asymmetric in plan, leads to unbalanced story-shear distribution, making roof displacement more sensitive to β and to the stiffness-reduction factor. The Multi-X layout provides multiple paths, but vertical force transfer spans several stories, allowing local degradation effects to accumulate with height. In contrast, the Chevron layout forms a "V" by connecting two braces at mid-span, offering parallel energy-dissipation paths, in-story closure of vertical resultants, and a short, symmetric load path. Consequently, when one member degrades, the companion member can share axial force, and unbalanced vertical components at the node are mitigated, reducing amplification of both local and global responses. Hence, over 0–120 cycles, the chevron scheme exhibits the smallest slope in the roof-displacement–versus-cycle curve and remains consistently below the other layouts, yielding the lowest normalized sensitivity index; the D-U and D-S schemes show markedly larger displacement growth with cycle count than the Multi-X and Chevron schemes (Table 8).

Table 8. Comparison of structural responses before and after brace performance degradation

Arrangement form	Maximum story drift ratio		Degradation rate /%	Maximum story shear /kN		Degradation rate /%	Top displacement /mm		Degradation rate /%
	Without considering performance degradation	Considering performance degradation		Without considering performance degradation	Considering performance degradation		Without considering performance degradation	Considering performance degradation	
D-S bracing	0.009114	0.010592	16.22	877.26	943.12	7.51	225.79	268.05	18.72
D-U bracing	0.00951	0.011761	23.67	901.15	971.11	7.76	231.23	286.64	23.96
Chevron bracing	0.00813	0.008223	1.14	806.26	822.56	2.02	190.77	200.99	5.36
Multi-story X bracing	0.007931	0.008872	11.87	999.31	1035.73	3.64	190.92	225.48	18.10

Note: Degradation rate = (Value considering performance degradation − Value without considering performance degradation) / Value without considering performance degradation.

6. Conclusions

This study conducted alternating high–low temperature hygrothermal cycling and subsequent quasi-static tests on six buckling-restrained braces (BRBs) with identical geometry and properties. The evolution of hysteretic behavior with cycle count was quantified, a modified Bouc–Wen model was developed to simulate the nonlinear hysteresis, and the impacts of brace performance degradation on frame systems with different bracing layouts were evaluated through time-history analysis. The main conclusions are:

Material and interface degradation: Hygrothermal cycling induces corrosion of the steel core and moisture ingress that weakens the bond at the core–unbonded layer interface, leading to slip under tension. The combined effects markedly reduce the tensile yield force, elastic stiffness, and ultimate tensile capacity of the brace.

Tension–compression asymmetry: Hygrothermal exposure accelerates the aging of the unbonded layer and diminishes its ability to suppress axial friction between the core and the restraining member, thereby elevating the compressive resistance. For the non-cycled specimen (BRB0), the maximum tension–compression asymmetry factor was 1.24 over the investigated amplitudes; for specimens subjected to ≥24 cycles, the factor at the design displacement $L/100$ clearly exceeded the code limit of 1.30, and it increased monotonically with both cycle count and displacement amplitude.

Modeling accuracy: The modified Bouc–Wen model reproduces cyclic hardening, stiffness degradation, and tension–compression asymmetry with good fidelity. The identified elastic stiffness K decreases with increasing cycle count, while the asymmetry factor β increases, consistent with the tests. A downward warping of the compressive branch appears at large compressive deformations, indicating that further refinement of the model structure is warranted to improve accuracy in this regime.

System-level effects: All four bracing layouts—single-diagonal symmetric, single-diagonal asymmetric, chevron (inverted-V), and multi-story X—substantially reduce seismic responses under maximum considered earthquakes; degradation amplifies response magnitudes but does not shift the weak-story location. Owing to its parallel energy-dissipation paths and in-story closure of vertical resultants, the chevron layout is least sensitive to degradation. After 120 cycles, the single-diagonal asymmetric scheme exhibits increases of 23.67% (peak interstory drift), 7.76% (peak story shear), and 23.96% (roof displacement), whereas the chevron scheme shows only 1.14%, 2.02%, and 5.36%, respectively

7. Declarations

7.1. Author Contributions

Conceptualization, Q.M. and K.X.; methodology, Q.M.; software, Y.L.; validation, Y.L., C.M., and J.Z.; formal analysis, Q.M. and Y.L.; investigation, Y.L. and C.M.; resources, Q.M. and K.X.; data curation, Y.L.; writing—original draft preparation, Q.M. and Y.L.; writing—review and editing, Y.L. and C.M.; visualization, J.Z.; supervision, Q.M. and K.X.; project administration, Q.M.; funding acquisition, Q.M. All authors have read and agreed to the published version of the manuscript.

7.2. Data Availability Statement

The data presented in this study are available on request from the corresponding author.

7.3. Funding

This research was supported by the National Natural Science Foundation of China (51208041) and the Natural Science Foundation of Shaanxi Province (2020SF-382, 2014JM2-5080). The supports are gratefully acknowledged.

7.4. Conflicts of Interest

The authors declare no conflict of interest.

8. References

[1] Talebi, E., Tahir, M. Md., Zahmatkesh, F., Yasreen, A., & Mirza, J. (2014). Thermal Behavior of Cylindrical Buckling Restrained Braces at Elevated Temperatures. The Scientific World Journal, 2014, 1–13. doi:10.1155/2014/672629.

[2] Hu, B., Xu, Y., Zhai, M., Wang, C., & Hu, W. (2024). Experimental study on the buckling restraint brace of low yield point steel 160 at different temperatures. Engineering Structures, 320, 118878. doi:10.1016/j.engstruct.2024.118878.

[3] Wei, X., Ngeljaratan, L., & Bruneau, M. (2019). Low-Cycle Fatigue of Buckling Restrained Braces in Bidirectional Ductile End Diaphragms Due to Temperature-Change Effect on Bridge Superstructure. Journal of Bridge Engineering, 24(4), 04019014. doi:10.1061/(asce)be.1943-5592.0001365.

[4] Wu, K., Wei, G., Zhang, L., Yu, W., & Lan, X. (2025). Experimental Study on the Seismic Behavior of All-Steel Buckling-Restrained Braces Without an Unbonded Material Layer. Buildings, 15(10), 1626. doi:10.3390/buildings15101626.

[5] Rahaei, A. R., Alinia, M. M., & Salehi, S. M. F. (2009). Cyclic Performance of Buckling Restrained Composite Braces Composed of Selected Materials. International Journal of Civil Engineering, 7(1), 1-8.

[6] Ostovar, N., & Hejazi, F. (2023). Buckling-Restrained Bracing System with Ultra-High-Performance Fiber Concrete. Applied Sciences, 13(14), 8250. doi:10.3390/app13148250.

[7] Ebanesar, A., Cruze, D., Noroozinejad Farsangi, E., Seenivasan, V. S. J., Mohammad, A. D., Abdul Rashid, D., & Gladston, H. (2019). Seismic Performance Evaluation of a Proposed Buckling-Restrained Brace for RC-MRFS. Civil and Environmental Engineering Reports, 29(3), 164–173. doi:10.2478/ceer-2019-0032.

[8] Bae, J., Ju, Y. K., & Oh, J. (2024). Cyclic Loading Test of Phase Change Material (PCM)-Infilled Buckling-Restrained Brace. International Journal of Civil Engineering, 22(12), 2233–2249. doi:10.1007/s40999-024-00986-x.

[9] Zaruma, S. R., & Fahnestock, L. A. (2018). Seismic Stability of Buckling-Restrained Braced Frames. Key Engineering Materials, 763, 924–931. doi:10.4028/www.scientific.net/KEM.763.924.

[10] Liu, Y., Li, H. N., Li, C., & Dong, T. Z. (2021). Lifetime seismic performance assessment of high-rise steel-concrete composite frame with buckling-restrained braces under wind-induced fatigue. Structural Engineering and Mechanics, 77(2), 197–215. doi:10.12989/sem.2021.77.2.197.

[11] Kabir, M. I., Shrestha, R., & Samali, B. (2016). Effects of applied environmental conditions on the pull-out strengths of CFRP-concrete bond. Construction and Building Materials, 114, 817–830. doi:10.1016/j.conbuildmat.2016.03.195.

[12] Fang, C., Cao, C., Xiao, Y., & Zheng, Y. (2023). Effect of corrosion on self-centering energy dissipative devices. Engineering Structures, 293, 116664. doi:10.1016/j.engstruct.2023.116664.

[13] Yan, B., Zhang, W., & Yi, W. (2024). Multi-scale study on the mechanical properties of concrete based on crack propagation under hygrothermal coupling. Journal of Building Engineering, 91, 109680. doi:10.1016/j.jobe.2024.109680.

[14] Ma, Q., Feng, D., Li, Y., Yao, B., & Wang, L. (2025). Mechanical Properties and Constitutive Model of Steel Under Temperature–Humidity Cycles. Buildings, 15(5), 732. doi:10.3390/buildings15050732.

[15] Zhou, Y., Shao, H., Cao, Y., & Lui, E. M. (2021). Application of buckling-restrained braces to earthquake-resistant design of buildings: A review. Engineering Structures, 246, 112991. doi:10.1016/j.engstruct.2021.112991.

[16] Wei, M., Ma, K., Yuan, B., Wei, Y., Chen, J., Tian, P., Zhao, B., & Sun, R. (2025). Cyclic behavior of a novel I-beams assembled buckling-restrained brace. Journal of Constructional Steel Research, 227, 109393. doi:10.1016/j.jcsr.2025.109393.

[17] Zong, L., Liu, H., Wang, J., & Ding, Y. (2024). Experimental and numerical investigation on mechanical and fatigue performance of corroded Q690D high-strength steel. Thin-Walled Structures, 195, 111466. doi:10.1016/j.tws.2023.111466.

[18] Bai, J., Chen, H., & Jin, S. (2021). Investigation on the interaction between BRBs and the RC frame in BRB-RCF systems. Engineering Structures, 243, 112685. doi:10.1016/j.engstruct.2021.112685.

[19] Jia, M., Lu, D., Guo, L., & Sun, L. (2014). Experimental research and cyclic behavior of buckling-restrained braced composite frame. Journal of Constructional Steel Research, 95, 90–105. doi:10.1016/j.jcsr.2013.11.021.

[20] Stewart, M. G., Wang, X., & Nguyen, M. N. (2011). Climate change impact and risks of concrete infrastructure deterioration. Engineering Structures, 33(4), 1326–1337. doi:10.1016/j.engstruct.2011.01.010.